Journal of Oceanology and Limnology

https://doi.org/10.1007/s00343-026-6002-y

Research Paper

Global estimating total suspended solids concentration in inland and coastal waters using deep learning*

Shen'ao HUANG[1, 2, 3], Xiaofeng LI[1, 2, 4], Dalin JIANG[5], Yi YANG[1, 2, 3], Xiaolong LI[1, 2, 4, **]

[1] *Key Laboratory of Ocean Observation and Forecasting, Institute of Oceanology, Chinese Academy of Sciences, Qingdao 266000, China*

[2] *Key Laboratory of Ocean Circulation and Waves, Institute of Oceanology, Chinese Academy of Sciences, Qingdao 266000, China*

[3] *University of Chinese Academy of Sciences, Beijing 101408, China*

[4] *Qingdao Key Laboratory of Artificial Intelligence Oceanography, Qingdao 266000, China*

[5] *Earth and Planetary Observation Sciences (EPOS), Biological and Environmental Sciences, Faculty of Natural Sciences, University of Stirling, Stirling FK9 4NH, United Kingdom*

Received Jan. 2, 2026; accepted in principle Apr. 3, 2026; accepted for publication Apr. 28, 2026

© Chinese Society for Oceanology and Limnology, Science Press and Springer-Verlag GmbH Germany, part of Springer Nature 2026

Abstract Total suspended solids (TSS) concentration is a fundamental indicator of water turbidity, sediment dynamics, and aquatic ecosystem health in inland and coastal waters. Accurate satellite-based TSS retrieval for those water bodies remains challenging due to their complex bio-optical conditions, high variability, and uncertainties in atmospheric correction. To address these challenges, we develop Total Suspended Solids Estimation Network (TSS-Net), a deep learning framework for global TSS estimation from multispectral remote-sensing reflectance (R_{rs}). TSS-Net employs a multi-layer feedforward architecture with residual connections to preserve spectral information and enhance model stability and generalization. A three-stage hierarchical training strategy is adopted by integrating radiative transfer simulations, global in-situ measurements, and Sentinel-2 MSI satellite observations. The radiative transfer simulations were used to physically constrain TSS-Net. Specifically, HydroLight-EcoLight 6 simulations are firstly used for pre-training to establish physically consistent R_{rs}-TSS relationships. The model is subsequently fine-tuned using a global representative in-situ dataset (1 776 samples) to capture real-world optical variability, and further adapted with 1 129 quality-controlled Sentinel-2 satellite matchups to mitigate satellite-specific uncertainties. Extensive evaluations demonstrate that TSS-Net consistently outperforms existing widely-used empirical, semi-analytical, and machine learning models, including the Jiang, MDN, and SOLID approaches. Evaluation using an independent global in-situ dataset, TSS-Net achieves R^2 of 0.84, mean absolute percentage error (MAPE) of 49.94%, and near-zero bias. When applied to Sentinel-2 matchups, it maintains strong performance (R^2=0.73, MAPE=37.39%), indicating robust generalization across diverse optical environments. Applications to the Upper Chesapeake Bay show that TSS-Net produces physically plausible TSS distribution patterns without region-specific recalibration. Overall, TSS-Net provides a robust, scalable, and generalizable solution for global TSS retrieval, supporting long-term water-quality monitoring.

Keyword: total suspended solid (TSS); color remote sensing; Sentinel-2; deep learning

1 INTRODUCTION

Total suspended solids (TSS) concentration is a key parameter for assessing water turbidity, underwater light conditions, and overall water quality. Variations in TSS modify the absorption and scattering of light within the water column,

* Supported by the Jing-Jin-Ji Regional Integrated Environmental Improvement-National Science and Technology Major Project of Ministry of Ecology and Environment of China (No. 2025ZD1201000), the National Natural Science Foundation of China (No. 42076200), and the Key Research and Development Program of Shandong Province (No. 2022CXPT020)

Academic Papers of the 28th Annual Meeting of the China Association for Science and Technology

** Corresponding author: lixiaolong@qdio.ac.cn

influencing the distribution of photosynthetically active radiation, primary productivity, sediment transport, resuspension processes, and the movement of nutrients and pollutants (Kirk, 1994; Bilotta and Brazier, 2008). TSS is also an important indicator for evaluating drinking-water safety, riverbed sediment loads, and the effectiveness of ecological restoration efforts (Palmer et al., 2005). Traditionally, TSS monitoring has relied on collecting water samples from vessels or fixed stations, followed by laboratory analysis. Although these methods provide high accuracy, they are labor-intensive, costly, and limited in spatial and temporal coverage, making them only applicable to a small number of specific sites. Constrained by labor and operational expenses, such approaches struggle to meet the demands of large-scale, continuous monitoring across broad spatial and temporal domains (Stroud et al., 2023).

Satellite ocean color remote sensing provides an important means for large-scale and near-real-time TSS monitoring. Medium-to-high spatial resolution sensors, such as the Sentinel-2 Multi-Spectral Instrument (MSI), offer suitable visible-to-near-infrared bands with spatial resolutions of 10–60 m, enabling the observation of both fine spatial patterns and variations in water constituents (Zhou et al., 2024). Previous studies have shown that TSS is highly sensitive to remote sensing reflectance R_{rs}, particularly in the green, red, and near-infrared bands (Nechad et al., 2010; Dogliotti et al., 2015). Based on these bands, empirical, semi-empirical, and semi-analytical models have been widely applied in inland, estuarine, and coastal waters, and several studies have developed more broadly applicable approaches for optically diverse waters (Dogliotti et al., 2015; Han et al., 2016; Jiang et al., 2021, 2023). Nevertheless, many empirical formulations remain calibrated for specific regions or optical conditions, which can limit their transferability (Wirabumi et al., 2021). Moreover, differences in particle characteristics can modify water optical properties and increase the difficulty of robust retrieval across contrasting environments (Liu et al., 2024a). Consequently, consistent TSS retrieval across waters with markedly different inherent optical properties (IOPs) remains challenging (Ouillon et al., 2008). In recent years, deep learning methodologies (Li et al., 2022, 2023; Wang et al., 2025) have been increasingly applied to ocean color remote sensing to capture the non-linear relationship between TSS and multi-band R_{rs} (Li et al., 2020; Ali et al., 2024; Kim et al., 2024). These methods outperform traditional models in accommodating complex non-linearities, handling high-dimensional spectral features, and extracting latent patterns from large datasets (Pahlevan et al., 2022). Nevertheless, most existing studies have been developed for a limited geographic area, resulting in training samples with restricted spatial coverage and insufficient optical diversity. Consequently, these models frequently have difficulties in maintaining consistent performance when applied to different water types (Jiang et al., 2023). Moreover, actual satellite observations are invariably influenced by factors such as sensor noise, uncertainties in atmospheric correction, and sub-pixel mixing (Stöffelmair et al., 2025). Without incorporating explicit constraints related to these physical processes, models are prone to overfitting localized samples and can exhibit substantial uncertainty when transferred across regions.

Radiative transfer simulation provides an effective way of alleviating the scarcity of in-situ measurements while incorporating physical priors into the retrieval process. Radiative transfer models like HydroLight-EcoLight 6 (HE60) (Mobley, 1994; Mobley and Sundman, 2008) can produce R_{rs} data across a broad spectrum of TSS concentrations, ranging from clear to highly turbid waters, based on defined IOPs, atmospheric boundary conditions, and geometric configurations (Pahlevan et al., 2020; Loisel et al., 2023). However, discrepancies remain between purely simulated data and actual satellite observations, particularly in regions with complex atmospheric conditions or highly variable coastal optical environments. Therefore, integrating simulated datasets with global field measurements and satellite matchup data is essential for developing a data-driven retrieval framework that is both physically guided and representative of diverse aquatic environments.

This study aims to develop a globally applicable deep learning model (TSS-Net) for retrieving TSS concentrations from multispectral R_{rs}. The main contributions are summarized as follows. First, we compiled three complementary R_{rs}-TSS datasets: (1) a HE60-simulated dataset generated under NEW CASE2 IOPs, spanning wide ranges of chlorophyll *a* (Chl *a*), CDOM, and inorganic particulate concentrations from clear to highly turbid waters; (2) a global in-situ measurement dataset covering estuaries, lakes, reservoirs, and coastal regions; and (3) a global Sentinel-2 satellite-observation dataset

processed with the Case 2 Regional Coast Colour (C2RCC) atmospheric correction, rigorously spatiotemporal matching with in-situ TSS, and subjected to comprehensive quality control. These datasets provide a robust foundation for model training and validation. Second, we propose a deep learning model, TSS-Net (TSS Estimation Network), which effectively captures the complex nonlinear relationships between multispectral R_{rs} and TSS concentration. Third, we design a phased training strategy consisting of pre-training using simulations, fine-tuning using in-situ measurements, and fine-tuning using satellite matchups. This framework allows the model to first learn a physically consistent R_{rs}-TSS mapping and subsequently adapt to observational variability prior to satellite application. Finally, we conduct a comprehensive global evaluation, comparing TSS-Net with widely-used existing models to assess its performance, robustness, and generalization across diverse aquatic environments.

2 DATA AND METHOD

2.1 Data compilation

2.1.1 Simulated dataset

The HE60 radiative transfer model was used to generate a TSS-R_{rs} dataset representative of diverse aquatic optical conditions, providing a physically grounded foundation for pre-training. The simulation rigorously complied with HE60 input criteria. The prescribed inputs to HE60 included the concentrations of Chl *a*, CDOM, and minerals, together with their associated optical settings. The output variables were R_{rs} at seven bands (490, 560, 665, 704, 740, 783, and 865 nm) and particle backscattering coefficients (b_{bp}).

The IOPs of the water column were described using the "NEW CASE2 IOPs" model which is designed to simulate the optical properties of optically complex Case-2 waters. Within the HE60 framework, absorption coefficients (*a*), scattering coefficients (*b*), and scattering phase functions can in general be defined as functions of wavelength and, when needed, depth. In the present study, however, no vertical stratification was simulated. Instead, the water column was assumed to be vertically homogeneous, with constant concentrations of Chl *a*, CDOM, and minerals throughout the water column. It should be noted that the simulated dataset does not represent mineral particles alone, but the combined optical contributions of three optically active components, namely Chl *a*, CDOM, and minerals, superimposed on a pure-water optical background under the NEW CASE2 IOP framework (Bi et al., 2023; Liu et al., 2024b). In the present HE60 setup, particle size cannot be directly prescribed as an independent input variable; therefore, particle size distribution was not explicitly parameterized in this study. Instead, the simulated optical conditions were defined through the concentrations of the major optical components, with particle-related scattering represented using the Petzold average-particle phase function (dpf_Petzold_avg_particle.txt). The absorption coefficient of pure water (a_w) were obtained from Pope and Fry (Pope and Fry, 1997), and the scattering coefficient (b_w) were obtained from the SEAWATER model. The absorption and scattering coefficients of inorganic minerals were specified using the default averaged mineral optical-property files in HE60, while particle scattering was represented through the particle phase function, which defines the volume scattering function as (Mobley, 1994):

$$\beta_p(\psi,\lambda) = b_p(\lambda)\tilde{\beta}_p(\psi,\lambda), \tag{1}$$

where $b_p(\lambda)$ is the particulate scattering coefficient and $\tilde{\beta}_p(\psi, \lambda)$ is the normalized particle phase function.

In this study, the particle phase function was specified as the Petzold average-particle phase function (Petzold, 1972; Hedley and Mobley, 2021). For phytoplankton-related particles, absorption was represented as (Prieur and Sathyendranath, 1981):

$$a_{ph}(\lambda) = C_{Chl\,a}\, a^*_{ph}(\lambda), \tag{2}$$

where $a^*_{ph}(\lambda)$ is the chlorophyll-specific absorption spectrum. Here, $a^*_{ph}(\lambda)$ was taken from the default chlorophyll-specific absorption file implemented in HE60 and follows the chlorophyll-specific spectral formulation reported by Prieur and Sathyendranath and Morel (Prieur and Sathyendranath, 1981; Morel, 1988; Hedley and Mobley, 2021). Chl-*a* absorption was simulated utilizing a conventional spectral curve featuring distinct peaks. Absorption coefficient of CDOM (a_{CDOM}) was represented as an exponential decay function contingent upon wavelength:

$$a_{CDOM}(\lambda) = a_{CDOM}(\lambda_0)\exp[-\gamma(\lambda-\lambda_0)]. \tag{3}$$

Here, λ_0 denotes the reference wavelength (440 nm), and the spectral slope parameter γ is set as 0.014.

The dataset covers clear to turbid waters, with simulations divided into five intervals based on Chl *a*, mineral concentrations, and $a_{CDOM}(440)$ (Table 1). These parameter ranges were adopted from previous synthetic-data-based TSS retrieval studies, particularly Jiang et al. (2021), to cover optical conditions spanning clear to extremely turbid waters. Compared with Jiang et al. (2021), the present study generated a substantially larger simulated dataset to provide stronger support for model pre-training. The dataset encompasses extensive ranges: Chl *a* from 0.01 to 1 000 mg/m^3, minerals from 0.01 to 1 000 g/m^3, and $a_{CDOM}(440)$ from 0.01 to 5/m. In each interval, component concentrations were aggregated using uniform random sampling, yielding 20 000 samples per interval, resulting in a cumulative total of 100 000 simulated samples.

TSS concentrations were calculated using the following formula:

$$\mathrm{TSS} = \alpha C_{\mathrm{Chl}\,a} + C_{\mathrm{minerals}}, \tag{4}$$

where $C_{\mathrm{chl}\,a}$ and C_{minerals} denote the concentrations of Chl *a* and minerals, respectively. The coefficient α denotes the proportional contribution of organic particles to the overall suspended mass. To augment the variability of TSS concerning optical components while preserving physical plausibility, α was designated values of 0.10, 0.15, 0.20, 0.25, and 0.30 for the five corresponding concentration intervals (Oyama et al., 2009; Xue et al., 2019).

The simulations utilized a multi-spectral setup, executing radiative transfer calculations over the seven specified bands to produce R_{rs}. Concerning boundary conditions, Raman scattering was disregarded, wind speed was established at 0 m/s, and the refractive index of water was maintained at n=1.34 for all bands. In HE60, particle refractive index was not varied as an independent input parameter. Instead, particle scattering was represented within the standard HE60 phase-function framework, and the particle phase function was specified as the Petzold average-particle phase function. The upper atmospheric boundary employed a semi-empirical sky irradiance model derived from RADTRAN-X, featuring a sun zenith angle of 30° and no cloud cover. An optically deep (infinitely deep) water column was assumed to ensure that bottom reflectance did not affect the simulated spectra.

Table 1 The range and quantity of chlorophyll-*a* concentration, minerals concentration and absorption coefficient of colored dissolved organic matter at 440 nm for simulations in this study

Range	Chl *a* (mg/m^3)	Mineral (g/m^3)	$a_{CDOM}(440)$ (/m)	Number
1	0.01–0.1	0.01–0.1	0.01–0.05	20 000
2	0.1–1	0.1–1	0.01–0.05	20 000
3	1–10	1–10	0.05–0.1	20 000
4	10–100	10–100	0.1–1	20 000
5	100–1 000	100–1 000	1–5	20 000

2.1.2 In-situ dataset

The in-situ dataset utilized in this study was sourced from various reputable water quality monitoring programs and research initiatives, including the Global Lake and River Observations database (GLORIA) (Lehmann et al., 2023), the U.S. Geological Survey (USGS) hydrological monitoring network, along with public research databases and literatures from Klotz et al. (2022) and Sadler et al. (2022). Sampling sites of the in-situ dataset are primarily located in inland and coastal water environments, including estuaries, lakes, and nearshore waters. These sites span a wide range of conditions—from highly turbid estuaries and port areas heavily influenced by human activities to relatively oligotrophic lakes and clear coastal waters. By integrating observational data from diverse water body types, the resulting dataset is broadly representative in both spatial distribution and hydro-optical characteristics.

The dataset comprises paired measurements of in-situ R_{rs} and TSS concentrations, exhibiting distinct spatiotemporal correlation. In the data compilation process, raw records from different sources were first harmonized by converting them into a unified file format, standardizing the target variable name as TSS, converting all TSS measurements to a consistent unit, and verifying the one-to-one correspondence between each TSS record and its associated R_{rs} spectrum. Records with missing key variables or physically implausible values were then removed. In addition, TSS concentrations were constrained to a reasonable range of 0.01–3 000 mg/L to reduce the influence of extreme outliers on model training and statistical analysis. The optical consistency of R_{rs} was assessed utilizing the Quality Water Index Polynomial (QWIP) method (Dierssen et al., 2022). To verify adherence to the essential physical limitations for aquatic remote sensing, spectra exhibiting an absolute QWIP score (|QWIP|)

greater than 0.2 were identified as outliers and excluded from the dataset.

Subsequent to the aforementioned screening and quality control procedures, a total of 1 776 valid samples were preserved in the final dataset. The dataset represents diverse waterways across North America, Europe, Asia, Oceania, Africa, and South America. It includes concentrated samples from the North American Great Lakes and European coastal waters, alongside high-latitude lakes and tropical estuaries, providing a comprehensive and globally representative baseline. The predominant samples are situated within the 1–100-mg/L range, indicative of the medium-to-low turbidity levels characteristic of most global lakes and coastal waters. A considerable quantity of observations for clean waters (TSS<1 mg/L) and severely turbid waters (TSS>100 mg/L) is also preserved (Fig.1a). The TSS distribution, covering various orders of magnitude, serves as a fundamental training dataset for the model's further training and generalization validation across a spectrum of optical conditions, from clear to turbid.

2.1.3 Satellite dataset

Satellite data from the European Space Agency's Sentinel-2 MSI sensor were used to construct a satellite R_{rs}-in-situ TSS matchup dataset and to evaluate model performance. A total of 297 images representing typical lakes, estuaries, and nearshore waters were acquired and processed, with native spatial resolutions ranging from 10 to 60 m. R_{rs} at seven spectral bands with center wavelengths of 490, 560, 665, 704, 740, 783, and 865 nm, were selected and resampled to a uniform 20-m resolution for use as spectral inputs to the inversion model, as these wavelengths are strongly correlated with key water-optical properties (Mamun et al., 2024; Paulino et al., 2025).

To guarantee the physical consistency and comparability of satellite reflectance, the C2RCC algorithm from SNAP (v10.0.0) was applied to perform atmospheric corrections on the Sentinel-2 Level-1C Top-of-Atmosphere reflectance data. C2RCC is specifically engineered for intricate nearshore and inland waters, concurrently estimating the contributions of non-algal particles (NAP), CDOM, and aerosols to the optical signal, thus obtaining R_{rs} that accurately reflects surface conditions (Brockmann et al., 2016).

Satellite imagery was matched to in-situ measurements under strict spatiotemporal consistency requirements. For construction of the satellite R_{rs}-in-situ TSS matchup dataset used for model training and evaluation, only Sentinel-2 images acquired on the same day as in-situ sampling and within a ±3-h temporal window were retained, thereby reducing uncertainties associated with short-term environmental change. For the independent evaluation of the agreement between C2RCC-corrected Sentinel-2 R_{rs} and in-situ R_{rs}, a stricter subset of synchronous matchups within ±1 h was

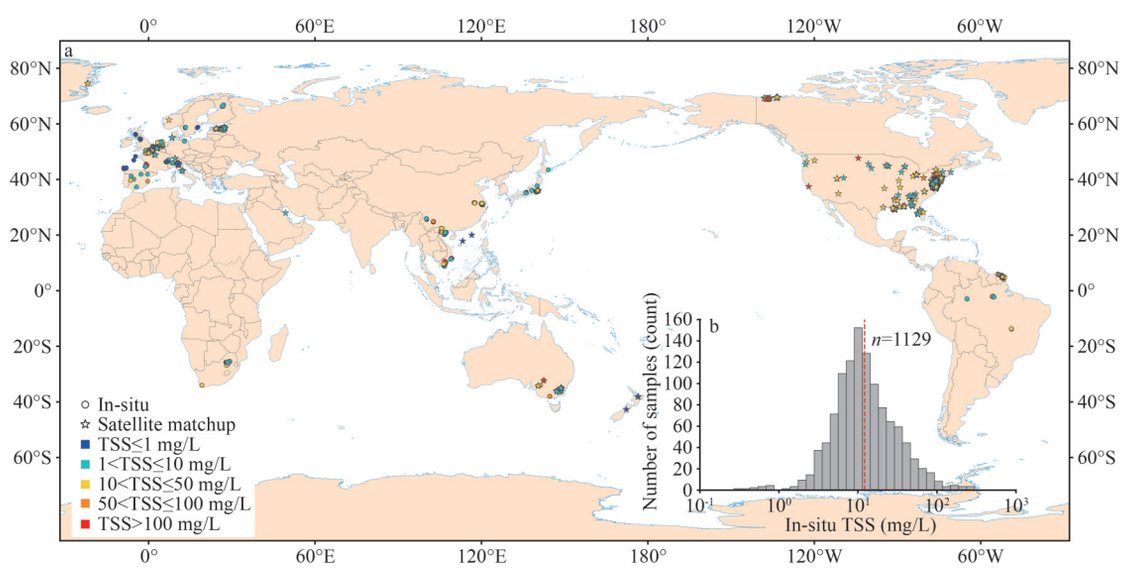


Fig.1 Spatial distribution of in-situ TSS samples and their satellite matchups (a), with subfigure (b) illustrating the TSS concentration distribution

Map review No. GS(2016)1667.

used to minimize additional spatiotemporal mismatch. Spatially, a 3×3 pixel neighborhood centered on each sampling station was extracted, and the mean R_{rs} value within this window was used to approximate the satellite observation, thereby reducing the effects of single-pixel noise and geolocation inaccuracies. To enhance the quality of the matching data, dual constraints were imposed on the 3×3 neighborhood surrounding each station: (1) each band must have a minimum of 3 genuine water pixels; and (2) the coefficient of variation (CV) of R_{rs} within the neighborhood must be below 0.5. Any station that did not satisfy either requirement was deemed as invalid match and excluded.

The comprehensive workflow encompasses atmospheric correction, band extraction, spatiotemporal alignment, and quality assurance (Fig.2). A high-quality satellite R_{rs}-in-situ TSS matchup dataset was acquired by rigorous screening, establishing a dependable basis for subsequent model refinement. A total of 1 129 valid matchup samples were retained after the above procedures (Fig1.b).

2.2 Method

This section presents the architecture of the proposed TSS-Net, its three-stage training strategy, and the evaluation metrics for model performance.

2.2.1 Model architecture

The architecture of TSS-Net (Fig.3) integrates multi-layer feedforward feature extraction, residual connections, and a regression output module. The model inputs are feature vectors composed of atmospherically corrected R_{rs} values at seven Sentinel-2 MSI bands. By learning the nonlinear mapping between multispectral R_{rs} and TSS, TSS-Net directly predicts TSS concentrations. In contrast to traditional empirical equations and semi-analytical models, TSS-Net employs a unified architecture capable of capturing the R_{rs}-TSS relationship across diverse regions and water types.

Prior to accessing the backbone network, these inputs are transformed into a high-dimensional feature space through a fully connected layer. The backbone consists of many sequential feedforward

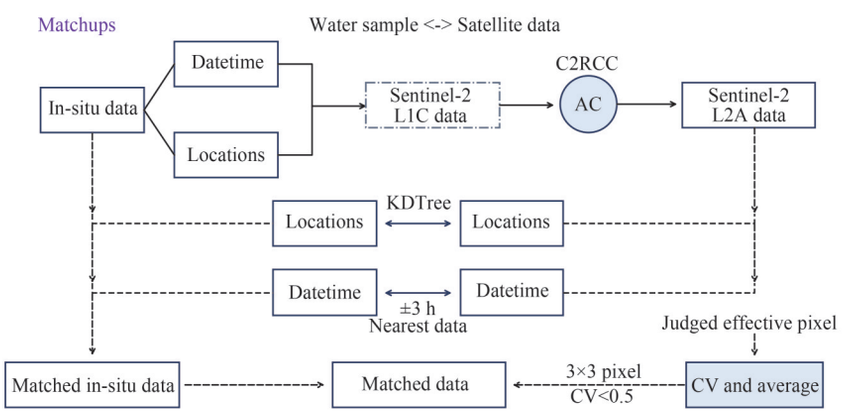


Fig.2 Schematic diagram of the in-situ satellite data matchup process

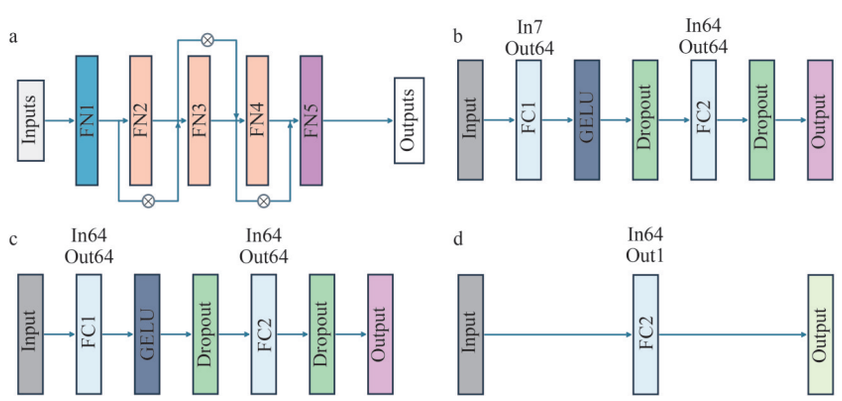


Fig.3 The TSS-Net model architecture and its core modules

a. schematic diagram of the overall model structure, including the Inputs layer (inputs), feature extraction modules (FN1–FN5), fully connected layer (FC), activation function (GELU), and Dropout layer; b. FN1 module structure; c. FN2–FN4 module structure; d. FN5 module (output layer) structure.

sub-networks (FN1–FN5). Every sub-network comprises a fully connected layer (FC), a non-linear activation function (Gaussian Error Linear Unit, GELU), and a Dropout layer. The GELU function preserves gradient stability while improving the network's sensitivity to minor non-linearities and nuanced spectral fluctuations. Dropout is employed to randomly deactivate a fraction of neurons, so suppressing overfitting and boosting the model's resistance to noise. The stacked feedforward architecture facilitates the hierarchical extraction of high-order composite characteristics from the original spectra, hence enhancing the exact characterization of the effects of different water color components and their combinations on TSS (Yin et al., 2024). Residual connections are established between neighboring feature sub-networks, as denoted by the "ⓧ" and arrows in Fig.3a. This design incorporates the feature representation from the previous layer straight into the output of the current layer using a shortcut connection. This effectively mitigates the vanishing and ballooning gradient issues frequently seen during the training of deep networks. Moreover, it maintains a direct pathway for superficial spectral information within the profound features, allowing the model to concurrently utilize local linear correlations and deep non-linear characteristics. This enhances training stability and generalization capacity (He et al., 2016; Liu et al., 2019). Ultimately, the high-dimensional features generated by the four feedforward sub-networks are fed into a final fully connected network (FC5), which executes feature compression and regularization using GELU and Dropout. The output layer has a linear regression node that directly forecasts the TSS concentration value. The network is trained using log-transformed TSS as the target variable, with the Mean Absolute Error (MAE) employed as the loss function.

2.2.2 Three-stage training strategy

TSS-Net employs a three-stage training framework consisting of pre-training on radiative transfer simulation data, fine-tuning on global in-situ data, and subsequent fine-tuning on satellite matchup data.

Stage 1: Pre-training with simulated data. TSS-Net is initially pre-trained using the simulated dataset. Both R_{rs} and TSS concentrations are transformed using logarithm with base 10, after which a StandardScaler is applied to normalize all variables to zero mean and unit variance. The seven standardized $\log_{10}(R_{rs})$ values serve as model inputs, while standardized $\log_{10}$(TSS) is used as the regression target. Training is conducted using full-batch learning (batch size equal to the total number of samples), a learning rate of 0.005, and 64 epochs. This phase enables the network to learn a physically consistent nonlinear mapping between R_{rs} spectra and TSS concentrations and establishes standardized scaling parameters for use in the subsequent training phases. Upon completion, the model weights and corresponding StandardScaler are saved for initialization during fine-tuning.

Stage 2: Fine-tuning with in-situ dataset. Using the pre-trained weights as initialization, the model is fine-tuned with a globally compiled in-situ TSS and R_{rs} dataset. Data standardization follows the same procedure as in Stage 1, maintaining consistent feature scaling throughout the training process. The in-situ dataset is then randomly divided into training and test subsets in an 8∶2 ratio. After loading the pre-trained weights, the model is optimized with a learning rate of 0.000 5 over 1 024 epochs. This phase adapts the network from the "physically plausible simulated spectral space" to real observational conditions, allowing it to better capture the complex R_{rs}-TSS relationships present in natural waters. The resulting optimized weights serve as the foundation for the next training phase.

Stage 3: Final fine-tuning with satellite matchup data. The base model is further fine-tuned using the satellite matchup dataset to enhance its applicability and robustness under real satellite observation conditions. All matchup samples are randomly divided into training and test sets in an 8∶2 ratio. The model from Phase 2 is used to initialize the weights, and training proceeds with a learning rate of 0.000 1 for 512 epochs. This phase is designed to reduce systematic effects of atmospheric-correction residuals, sensor response differences, and satellite noise on the R_{rs}-TSS relationship, thereby guiding TSS-Net toward optimal parameter convergence within the Sentinel-2 observation framework.

TSS-Net employs a three-stage training process, "physical simulation-in-situ measurements-satellite observations", implemented entirely within the PyTorch framework using the Adam optimizer. This strategy preserves the physical consistency provided by radiative transfer simulations while progressively integrating the real water optical characteristics captured in in-situ measurements and satellite observations.

2.2.3 Accuracy assessment

To comprehensively assess the retrieval performance of TSS-Net, five metrics were employed: the Coefficient of Determination (R^2), Root Mean Square Error (RMSE), Root Mean Square Logarithmic Error (RMSLE), Mean Absolute Percentage Error (MAPE), and Bias.

$$R^2 = 1 - \frac{\sum_{i=1}^{n}(y_i - \hat{y}_i)^2}{\sum_{i=1}^{n}(y_i - \bar{y})^2}, \tag{5}$$

$$\mathrm{RMSE} = \sqrt{\frac{1}{n}\sum_{i=1}^{n}(y_i - \hat{y}_i)^2}, \tag{6}$$

$$\mathrm{RMSLE} = \sqrt{\frac{1}{n}\sum_{i=1}^{n}\left[\log_{10}(y_i + 1) - \log_{10}(\hat{y}_i + 1)\right]^2}, \tag{7}$$

$$\mathrm{MAPE} = \frac{100\%}{n}\sum_{i=1}^{n}\left|\frac{y_i - \hat{y}_i}{y_i}\right|, \tag{8}$$

$$\mathrm{Bias} = \frac{1}{n}\sum_{i=1}^{n}(\hat{y}_i - y_i), \tag{9}$$

where, y_i signifies the in-situ measured TSS for the i^{th} sample, $\hat{y}_i$ denotes the corresponding predicted value obtained from the model, $\bar{y}$ is the mean of the observed TSS, and n indicates the total number of samples.

3 RESULT

3.1 Validation using global in-situ data

To evaluate the cross-regional generalization capacity of TSS-Net, we tested the model utilizing an independent worldwide in-situ dataset (n=356) that was completely excluded from the training process. This dataset spans multiple water types and covers a wide range of TSS concentrations (10^{-2}–10^3 mg/L). For comparison, three representative existing TSS retrieval methods were selected as benchmarks, namely the Jiang model (Jiang et al., 2023), the MDN model (Pahlevan et al., 2020), and SOLID (Balasubramanian et al., 2020). These three methods were chosen because they represent three methodological directions in current TSS retrieval research, including a semi-analytical method, a machine-learning method based on a Mixture Density Network, and a hybrid framework combining water-type classification, optical constituent retrieval, and conditional TSS estimation. The comparison results are shown in Fig.4. In the figure, both axes employ logarithmic scales, and the fitting lines and statistical metrics were derived using $\log_{10}$(TSS) to attenuate the influence of extreme values and provide uniform assessment across models.

TSS-Net had superior performance compared to the three existing models across all statistical indicators. The coefficient of determination (R^2= 0.843) was substantially higher than those of the Jiang (0.690), MDN (0.790), and SOLID (0.761) models, signifying a greater ability to elucidate observational variation. The RMSE (0.259) and RMSLE (0.522) of TSS-Net were smaller than the other three methods. TSS-Net also obtained a MAPE of 49.94% for relative error, significantly outperforming Jiang (85.49%), MDN (62.18%), and SOLID (73.31%). The bias of -0.002 indicates that TSS-Net predictions are closely aligned with the 1∶1 reference line throughout the whole dynamic range without substantial overestimations or underestimations. Although the comparison models also exhibit small bias values, they were associated with elevated RMSE, RMSLE, and MAPE, indicating that the relative errors of their predictions have increased.

The scatter distribution further illustrates these differences. The scatter points for TSS-Net cluster tightly around the 1∶1 line, particularly within the low-to-medium concentration range (1–100 mg/L), contributing to its high R^2 value. The regression slope of 0.849, being somewhat less than 1, suggests a modest underestimation at higher TSS values, though the deviation is small and the overall fit remains stable. In contrast, the regression slope of the Jiang model (1.006) approximates the ideal 1∶1 connection; however, it exhibits a high MAPE due to multiple pronounced outliers in the elevated TSS range, leading to greater RMSE, RMSLE, and MAPE compared to TSS-Net. The MDN and SOLID models exhibit regression slopes of 0.739 and 0.792, respectively, indicating clear “slope compression”. These results in systematic underestimation at the high end and an overestimation at the low end, notably noticeable in the low-value zone (TSS<1 mg/L), where predictions tend to converge around 1 mg/L, thereby inflating their MAPE and RMSLE.

In general, TSS-Net surpasses the Jiang, MDN, and SOLID models in both variance explanation and error magnitude, delivering more balanced and robust

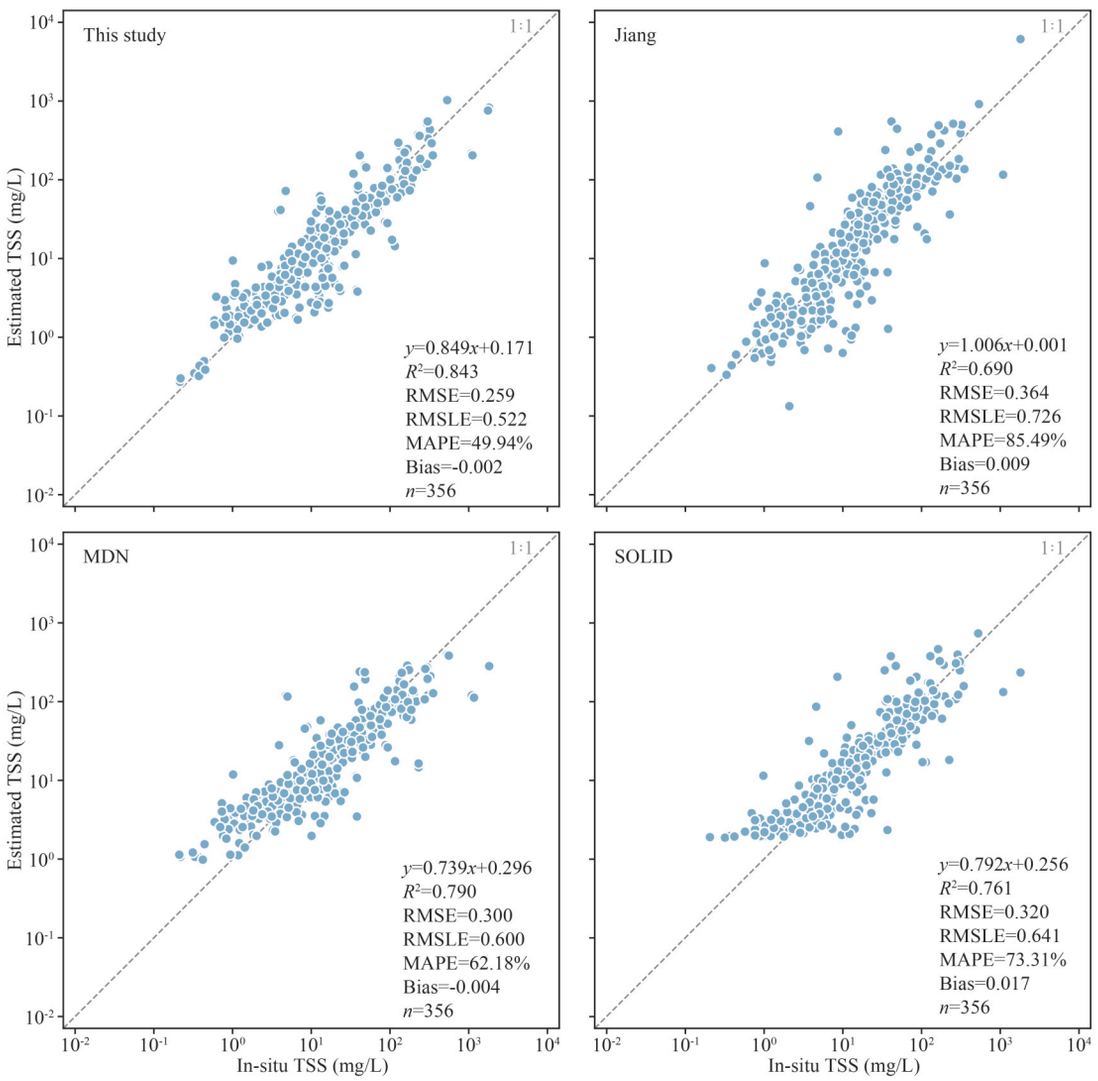


Fig.4 Comparisons between in situ measurements and estimated TSS using TSS-Net proposed in this study, Jiang (Jiang et al., 2023), MDN (Pahlevan et al., 2020), and SOLID (Balasubramanian et al., 2020)

performance across a broad range of TSS concentrations spanning multiple orders of magnitude.

3.2 Performance evaluation with satellite matchup data

To assess the performance of TSS-Net under satellite observation conditions, we conducted an independent validation utilizing a matched dataset comprising Sentinel-2 MSI R_{rs} and global in-situ TSS (n=226). Results were also compared with the Jiang, MDN, and SOLID models (Fig.5).

TSS-Net showed the strongest performance among all models. The coefficient of determination (R^2=0.726) surpassed that of the Jiang (0.538), MDN (0.691), and SOLID (0.631) models, signifying that TSS-Net can elucidate a greater share of observational variance despite the incorporation of uncertainties like atmospheric correction errors and sensor noise. TSS-Net attained the minimal RMSE=0.207 and RMSLE=0.436, indicating a more convergent error magnitude and distribution in logarithmic space along the concentration gradient. The MAPE was 37.39%, which is lower than Jiang's 40.81%, MDN's 45.30%, and SOLID's 52.23%. The bias (-0.019) was nearly negligible, suggesting that the model does not demonstrate substantial consistent overestimation or underestimate in satellite observations.

The spatial pattern of scatter points further highlights these differences. For TSS-Net, scatter points remain tightly concentrated around the 1:1 line with a nearly symmetric distribution. The

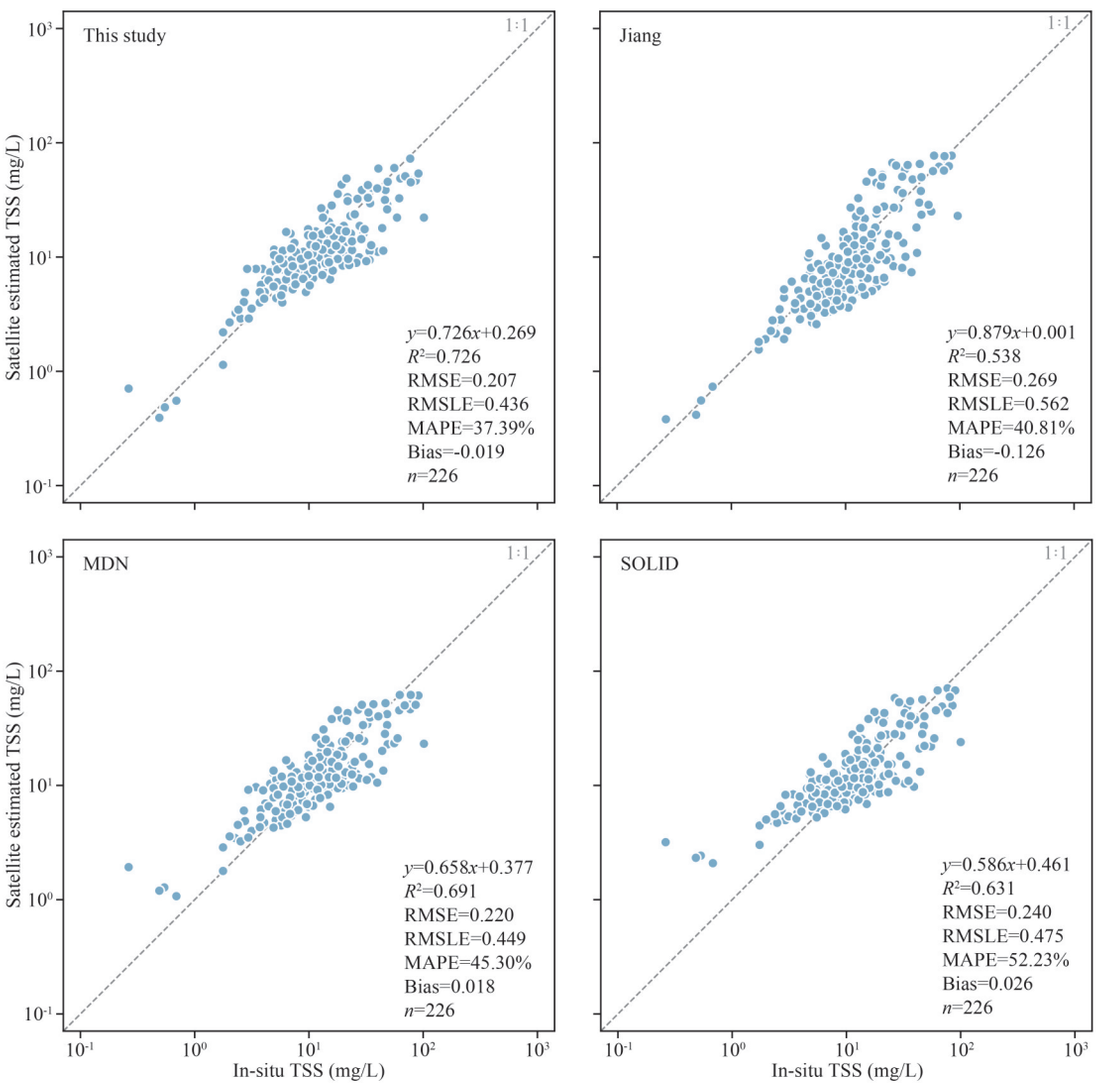


Fig.5 Comparisons between in-situ TSS and satellite-retrieved TSS using the TSS-Net proposed in this study, Jiang (Jiang et al., 2023), MDN (Pahlevan et al., 2020), and SOLID (Balasubramanian et al., 2020)

regression line (y=0.726x+0.269) has a slope slightly lower than 1, reflecting modest underestimation at higher TSS values; however, the overall alignment with the 1∶1 line indicates stable retrieval performance under real satellite measurements. In contrast, the Jiang model's regression line (y=0.879x+0.001) appears closer to the ideal slope, yet its scatter pattern shows greater spread, especially in the medium-to-high concentration range, leading to significantly elevated RMSE, RMSLE, and MAPE values. Its higher negative bias (-0.126) indicates a more pronounced systematic underestimation than TSS-Net. The MDN and SOLID models show more slope flattening (0.658 and 0.586, respectively), suggesting that both models tend to underestimate high TSS concentrations while simultaneously overestimating the lowest concentration values. Their respective MAPE (45.30% and 52.23%) and RMSLE exceed those of TSS-Net, indicating an inadequate sensitivity to spectral variations under conditions of low reflectance and poor signal-to-noise ratio. Overall, TSS-Net achieves a better fit and lower errors than the Jiang, MDN, and SOLID models in the satellite matchup evaluation.

3.3 Ablation experiment

An ablation study was performed to systematically assess the effects of the proposed architectural components and the three-stage training strategy by benchmarking the TSS-Net against four variants: "w/o Residual" (without residual connections), "w/o Pre-training" (without simulation-based initialization), "w/o In-situ

Tuning" (without fine-tuning on global in-situ data), and "w/o Sat-tuning" (without fine-tuning on satellite matchup data).

The comparison results for the independent in-situ validation dataset and the Sentinel-2 matchup dataset are summarized in Table 2. On the in-situ validation dataset, the architectural ablation revealed that the "w/o Residual" variant suffered a marginal performance degradation, with RMSE increasing by approximately 0.003 and R^2 decreasing slightly by 0.003. This suggests that residual connections contribute to optimization efficiency and feature propagation, the model's fundamental representation capacity is primarily driven by the feature extraction backbone. Notably, the "w/o In-situ Tuning" variant displayed a catastrophic performance collapse. Without fine-tuning on global in-situ data, the RMSE surged by 132.4% (from 0.259 to 0.602), and the explanatory power (R^2) plummeted by 81.9% (from 0.843 to 0.153). This dramatic degradation highlights the fundamental gap between theoretical radiative transfer simulations and real-world observations. Although simulation-based pre-training establishes a physically guided initialization, synthetic datasets alone cannot fully represent the complex bio-optical properties of natural waters. Consequently, the in-situ fine-tuning stage is essential for bridging this gap and achieving reliable TSS retrieval performance.

A similar pattern emerges in the satellite matchup evaluation. The failure of the model variant without satellite fine-tuning underscores the necessity of the final training stage and reveals the discrepancies between in-situ and satellite-derived R_{rs}. As shown in Table 2, this variant yields a negative R^2 (-0.17) and a pronounced negative bias (-0.304), indicating a complete loss of predictive skill. This outcome delineates the limits of model transferability: even a model that performs well on in-situ data (R^2=0.843) may fail to generalize to satellite observations without explicit adaptation. Such failures arise from atmospheric correction residuals, sensor signal-to-noise limitations, and spectral inconsistencies induced by spatial scale effects.

Table 2 Ablation study of different training strategies on in-situ and satellite datasets

Dataset	Method	R^2	RMSE	MAPE (%)	Bias
In-situ	Full	0.843	0.259	49.94	-0.002
	w/o Residual	0.840	0.262	48.68	-0.011
	w/o Pre-training	0.838	0.263	52.06	0.009
	w/o In-situ Tuning	0.153	0.602	119.35	-0.253
Satellite matchup	Full	0.726	0.207	37.39	-0.019
	w/o Residual	0.722	0.209	37.68	-0.021
	w/o Pre-training	0.724	0.208	38.06	-0.013
	w/o In-situ Tuning	0.722	0.209	36.25	-0.038
	w/o Sat-tuning	-0.17	0.428	54.73	-0.304

Overall, simulation pre-training and in-situ fine-tuning serve as essential intermediate steps that progressively improve TSS-Net's performance, the intrinsic differences among simulated data, field measurements, and satellite observations necessitate targeted fine-tuning for the final application domain. Only through this hierarchical training strategy can TSS-Net achieve robust and transferable performance across data sources.

4 APPLICATION OF TSS-NET IN CHESAPEAKE BAY

To demonstrate the capability of TSS-Net in producing reasonable spatial distributions of TSS, the upper Chesapeake Bay was selected as a case-study region. This region is characterized by significant spatiotemporal variability in sediment loads driven by tidal forcing and freshwater inputs (Fugate and Friedrichs, 2003; Ondrusek et al., 2012). Four Sentinel-2 MSI images acquired between August 2018 and April 2019 were processed using the C2RCC atmospheric correction algorithm and subsequently input into TSS-Net to produce instantaneous TSS distribution maps (Fig.6). These acquisition dates were chosen to enable direct comparison with the results reported by Balasubramanian et al. (2020). The TSS-Net outputs successfully capture the gradient characteristic from estuary-to-bay, with suspended matter concentrations decreasing seaward, and clearly distinguish TSS distribution patterns under different hydrological conditions. For instance, the widespread high TSS value observed on February 25, 2019, aligns with the high-flow event recorded by Balasubramanian et al. (2020), whereas the images from August 29, 2018, and April 6, 2019, exhibit low background levels typical of calmer hydrological conditions.

It is worth noting that this study employs the C2RCC atmospheric correction processor, whereas Balasubramanian et al. (2020) used the ACOLITE algorithm. Although differences in atmospheric correction approaches may lead to discrepancies in

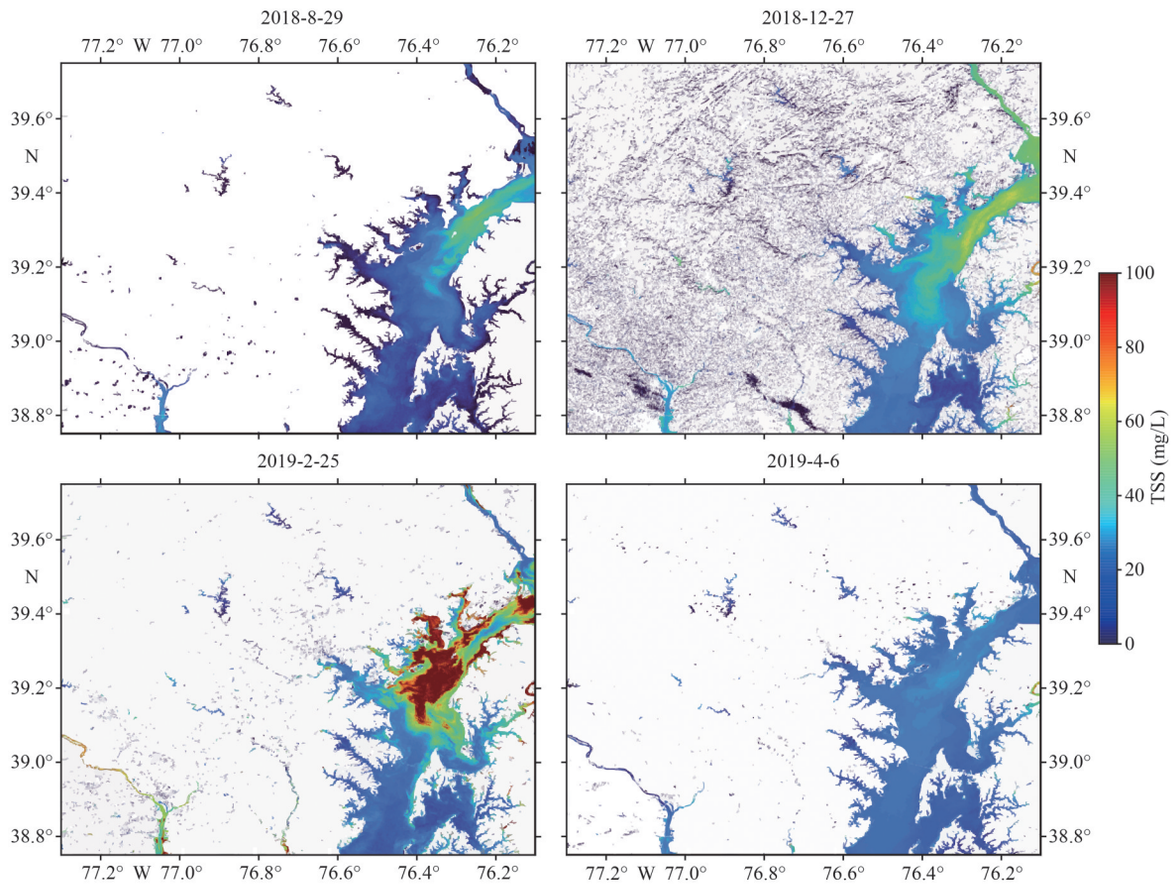


Fig.6 Spatiotemporal distributions of TSS in the Upper Chesapeake Bay derived from TSS-Net using Sentinel-2 MSI imagery acquired on August 29, 2018, December 27, 2018, February 25, 2019, and April 6, 2019

absolute TSS magnitude, the spatial patterns retrieved by TSS-Net are highly consistent with those reported in previous studies (Balasubramanian et al., 2020). In particular, TSS-Net reproduces spatial textures and transition features comparable to those obtained using regional empirical models (Ondrusek et al., 2012) and the SOLID algorithm (Balasubramanian et al., 2020). This agreement indicates that TSS-Net, trained on globally diverse data, has the great potential to be applied without regional fine-tuning, highlighting its robustness in complex aquatic systems.

5 DISCUSSION

TSS-Net is a deep learning framework designed to retrieve TSS concentrations across global aquatic environments. The model adopts a three-stage training strategy that integrates radiative transfer simulations, global in-situ measurements, and Sentinel-2 satellite observations. Compared with existing TSS retrieval approaches, TSS-Net achieves consistently higher accuracy on both independent global in-situ and satellite matchup datasets, outperforming benchmark models such as Jiang, MDN, and SOLID (Balasubramanian et al., 2020; Pahlevan et al., 2020; Jiang et al., 2023). Compared with the semi-analytical Jiang model, TSS-Net is more flexible in capturing complex nonlinear R_{rs}-TSS relationships, although it is less directly interpretable in physical terms. Compared with SOLID, TSS-Net avoids the stepwise conditional retrieval pathway, whereas SOLID is more transparent in its use of water-type classification and constituent-based retrieval logic. Compared with MDN, whose primary strength lies in probabilistic modeling, TSS-Net places greater emphasis on staged adaptation from simulated data to in-situ and satellite observations, while also achieving higher accuracy in TSS estimation. Ablation experiments on the three-stage training framework demonstrate that fine-tuning for the target application scenario is essential to the performance of TSS-Net, highlighting substantial differences in the R_{rs}-TSS mapping relationships among simulated, in-situ, and satellite-

observed data. By progressively transitioning from simulation-based pre-training to in-situ and satellite-specific fine-tuning, the three-stage framework enhances the robustness of TSS-Net and enables the effective integration of physical prior knowledge into a data-driven modeling approach.

Because accurate R_{rs} forms the physical foundation of TSS estimation, the performance of TSS-Net remains inherently constrained by the quality of the input R_{rs}, even with satellite-specific fine-tuning. Previous studies (Brockmann et al., 2016; Jiang et al., 2023) have shown that the C2RCC algorithm generally outperforms other commonly used MSI atmospheric correction processors, such as ACOLITE, Polymer, and Sen2Cor; accordingly, C2RCC was adopted in this study. Figure 7 compares C2RCC-corrected satellite spectra with synchronous in-situ R_{rs} measurements. Although C2RCC reproduces the overall spectral shape of water bodies and preserves general consistency with observations, the satellite-derived R_{rs} exhibits a systematic underestimation and a compressed dynamic range relative to the measured data (Renosh et al., 2020; Liu et al., 2022). This underestimation is particularly pronounced at 490 and 560 nm, where the distribution centers of satellite values are markedly shifted toward lower reflectance. Similar underestimation is also evident at 704 nm and longer wavelengths. The presence of consistent bias across all bands suggests that C2RCC may overestimate aerosol scattering or overcorrect atmospheric radiance, thereby limiting its ability to fully recover the true R_{rs} (Pahlevan et al., 2021).

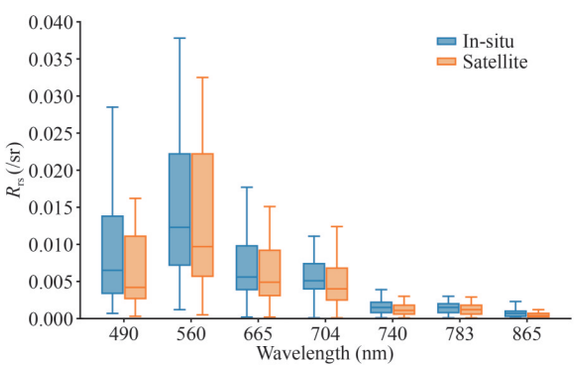


Fig.7 Comparison between in-situ and Sentinel-2 R_{rs} distributions across spectral bands

Figure 8 further illustrates band-specific discrepancies in R_{rs} accuracy. Although satellite and in-situ R_{rs} exhibit consistent overall trends across all seven bands, the global regression slope is only 0.76, and the MAPE reaches 109.6%, indicating underestimations and substantial relative error. At 490 nm, the regression slope decreases to 0.64, implying an approximate 36% signal loss in satellite observations. At 740 and 783 nm, the regression slopes further decreased to 0.43 and 0.41, respectively. The two data points with in-situ R_{rs}> 0.01/sr are clearly underestimated, indicating the failure of C2RCC in highly turbid waters. Because

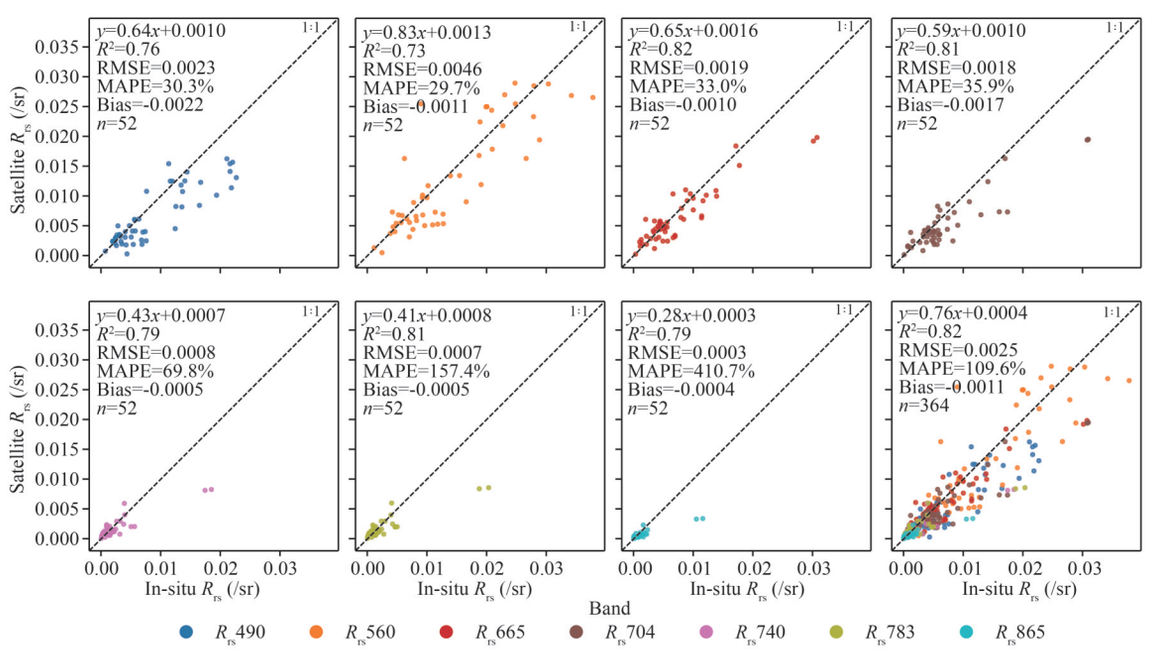


Fig.8 Band-specific relationships between in-situ and C2RCC-corrected Sentinel-2 R_{rs} across spectral bands

water-leaving radiance is intrinsically weak at longer wavelengths, even small absolute errors can translate into large relative biases. Consequently, the MAPE exceeds 60% in the 740 nm, 783 nm, and 865 nm bands, undermining the reliability of satellite-derived inputs and, in turn, TSS retrieval accuracy. It should be noted that the discrepancies between in-situ and satellite R_{rs} do not originate from atmospheric correction alone, but also include unavoidable spatiotemporal matchup uncertainty, although the use of a stricter ±1-h subset helped reduce this source of mismatch.

To investigate how band-specific R_{rs} errors may affect model performance, we conducted a permutation feature importance (PFI) analysis (Breiman, 2001; Fisher et al., 2019). Robustness testing based on 30 repeated experiments (Fig.9) shows that TSS-Net relies unevenly on different spectral bands. Notably, the 490 nm (20.6%) and 740 nm (19.5%) bands together account for nearly 40% of the model's decision weight, while both bands exhibit systematic underestimation in satellite observations to varying degrees (Figs.7 & 8). This imbalance likely contributes to the degradation in satellite-based performance relative to in-situ validation (Figs.4 & 5), suggesting that band-dependent uncertainties in satellite-derived R_{rs} may influence the final TSS estimates in a non-uniform manner. However, this inference remains qualitative, and a dedicated error-propagation analysis from R_{rs} uncertainty to TSS retrieval error was beyond the scope of the present study.

In summary, although TSS-Net demonstrates strong capability in learning complex R_{rs}-TSS relationships, its performance in satellite applications is ultimately constrained by the accuracy of atmospheric correction. In particular, uncertainties in key bands, especially 490, 560, and 740 nm, are therefore likely important contributors to the residual errors in satellite-based TSS retrieval. These findings emphasize that further improvements in atmospheric correction and uncertainty-aware modeling are essential to realize the potential of deep-learning-based TSS inversion.

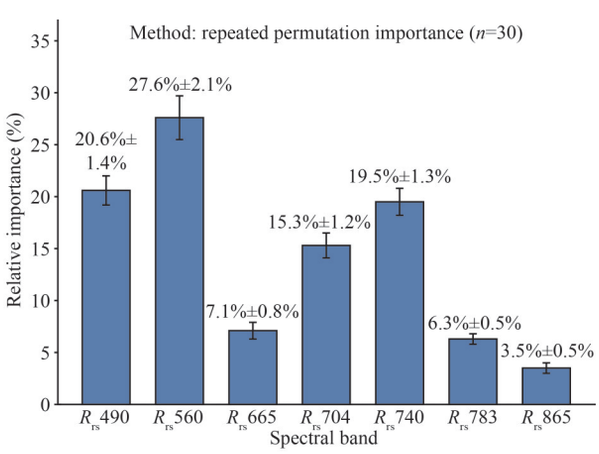


Fig.9 Relative importance of spectral bands for TSS-Net derived from PFI analysis

A dedicated error-propagation analysis to quantify how R_{rs} uncertainties translate into TSS retrieval error was beyond the scope of the present study. Future work will explicitly examine how band-specific R_{rs} uncertainties propagate to TSS retrieval error under satellite observation conditions.

6 CONCLUSION

This study presents TSS-Net, a physically guided deep learning framework for estimating TSS in global inland and coastal waters from multispectral R_{rs}. By integrating radiative transfer simulations, global in-situ measurements, and Sentinel-2 satellite observations within a three-stage hierarchical training strategy, TSS-Net effectively bridges the gap between theoretical optical modeling and real-world satellite applications.

Comprehensive validation demonstrates that TSS-Net consistently outperforms widely used benchmark models, including the Jiang, MDN, and SOLID approaches, across both independent global in-situ datasets and satellite matchup datasets. The model achieves lower error magnitudes and more balanced performance across multiple orders of magnitude in TSS concentration, from optically clear waters to highly turbid environments. These results highlight the strong cross-regional generalization capability of TSS-Net and its suitability for large-scale, operational water-quality monitoring.

Ablation experiments further reveal that fine-tuning to the target data domain is essential for reliable TSS retrieval. While simulation-based pre-training provides a physically consistent initialization, it alone is insufficient to capture the complex bio-optical variability of natural waters. In-situ fine-tuning is critical for adapting the model to real optical conditions, and satellite-specific fine-tuning is indispensable for mitigating atmospheric correction residuals, sensor noise, and scale-related inconsistencies.

Application of TSS-Net to the Upper Chesapeake Bay demonstrates that the model can generate

physically plausible TSS distribution patterns without regional recalibration. The retrieved distributions successfully reproduce known estuary-to-bay gradients and hydro-dynamically driven variability, and are consistent with results reported by previous regional and semi-analytical studies, underscoring the robustness of TSS-Net.

Despite its strong performance, the study also highlights a key limitation: the accuracy of TSS-Net under satellite observation conditions remains constrained by the quality of atmospheric correction, particularly in spectrally important bands such as 490, 560, and 740 nm. PFI analysis shows that biases in these high-impact bands are likely reflected in the TSS estimates to different extents. Future improvements in atmospheric correction algorithms, uncertainty-aware modeling, and joint retrieval frameworks are therefore essential to further enhance deep-learning-based TSS inversion.

In summary, TSS-Net provides a robust, scalable, and physically grounded solution for global TSS retrieval from satellite observations. The three-stage training framework offers a method for integrating physical priors into data-driven remote sensing models and can be readily extended to other water-quality parameters and sensors, supporting long-term, large-scale aquatic environment monitoring and management.

7 DATA AVAILABILITY STATEMENT

The datasets generated and/or analyzed during this study are available from the corresponding author on reasonable request.

8 ACKNOWLEDGMENT

We sincerely appreciate the editorial team and reviewers for their careful evaluation and valuable feedback.

References

Ali A, Zhou G H, Pablo Antezana Lopez F et al. 2024. Deep learning for water quality multivariate assessment in inland water across China. *International Journal of Applied Earth Observation and Geoinformation*, **133**: 104078, https://doi.org/10.1016/j.jag.2024.104078.

Balasubramanian S V, Pahlevan N, Smith B et al. 2020. Robust algorithm for estimating total suspended solids (TSS) in inland and nearshore coastal waters. *Remote Sensing of Environment*, **246**: 111768, https://doi.org/10.1016/j.rse.2020.111768.

Bi S, Hieronymi M, Röttgers R. 2023. Bio-geo-optical modelling of natural waters. *Frontiers in Marine Science*, **10**: 1196352, https://doi.org/10.3389/fmars.2023.1196352.

Bilotta G S, Brazier R E. 2008. Understanding the influence of suspended solids on water quality and aquatic biota. *Water Research*, **42**(12): 2849-2861, https://doi.org/10.1016/j.watres.2008.03.018.

Breiman L. 2001. Random forests. *Machine Learning*, **45**(1): 5-32.

Brockmann C, Doerffer R, Peters M et al. 2016. Evolution of the C2RCC neural network for Sentinel 2 and 3 for the retrieval of ocean colour products in normal and extreme optically complex waters. *In*: Living Planet Symposium 2016. Prague. p.54.

Dierssen H M, Vandermeulen R A, Barnes B B et al. 2022. QWIP: a quantitative metric for quality control of aquatic reflectance spectral shape using the apparent visible wavelength. *Frontiers in Remote Sensing*, **3**: 869611, https://doi.org/10.3389/frsen.2022.869611.

Dogliotti A I, Ruddick K G, Nechad B et al. 2015. A single algorithm to retrieve turbidity from remotely-sensed data in all coastal and estuarine waters. *Remote Sensing of Environment*, **156**: 157-168, https://doi.org/10.1016/j.rse.2014.09.020.

Fisher A, Rudin C, Dominici F. 2019. All models are wrong, but *Many* are useful: learning a variable's importance by studying an entire class of prediction models simultaneously. *Journal of Machine Learning Research*, **20**(177): 1-81.

Fugate D C, Friedrichs C T. 2003. Controls on suspended aggregate size in partially mixed estuaries. *Estuarine, Coastal and Shelf Science*, **58**(2): 389-404, https://doi.org/10.1016/S0272-7714(03)00107-0.

Han B, Loisel H, Vantrepotte V et al. 2016. Development of a semi-analytical algorithm for the retrieval of suspended particulate matter from remote sensing over clear to very turbid waters. *Remote Sensing*, **8**(3): 211, https://doi.org/10.3390/rs8030211.

He K M, Zhang X Y, Ren S Q et al. 2016. Deep residual learning for image recognition. *In*: Proceedings of the 2016 IEEE Conference on Computer Vision and Pattern Recognition. IEEE, Las Vegas. p.770-778, https://doi.org/10.1109/CVPR.2016.90.

Hedley J D, Mobley C D. 2021. Hydrolight 6.0 Ecolight 6.0 Technical Documentation. Numerical Optics Ltd., Tiverton, 131p.

Jiang D L, Matsushita B, Pahlevan N et al. 2021. Remotely estimating total suspended solids concentration in clear to extremely turbid waters using a novel semi-analytical method. *Remote Sensing of Environment*, **258**: 112386, https://doi.org/10.1016/j.rse.2021.112386.

Jiang D L, Matsushita B, Pahlevan N et al. 2023. Estimating the concentration of total suspended solids in inland and coastal waters from Sentinel-2 MSI: a semi-analytical approach. *ISPRS Journal of Photogrammetry and Remote Sensing*, **204**: 362-377, https://doi.org/10.1016/j.isprsjprs.2023.09.020.

Kim D, Lee K, Jeong S et al. 2024. Real-time chlorophyll-*a* forecasting using machine learning framework with

dimension reduction and hyperspectral data. *Environmental Research*, **262**(Pt 1): 119823, https://doi.org/10.1016/j.envres.2024.119823.

Kirk J T O. 1994. Light and Photosynthesis in Aquatic Ecosystems. 2nd edn. Cambridge University Press, Cambridge. 509p.

Klotz D, Kratzert F, Gauch M et al. 2022. Uncertainty estimation with deep learning for rainfall-runoff modeling. *Hydrology and Earth System Sciences*, **26**(6): 1673-1693, https://doi.org/10.5194/hess-26-1673-2022.

Lehmann M K, Gurlin D, Pahlevan N et al. 2023. GLORIA-A globally representative hyperspectral in situ dataset for optical sensing of water quality. *Scientific Data*, **10**(1): 100, https://doi.org/10.1038/s41597-023-01973-y.

Li X F, Liu B, Zheng G et al. 2020. Deep-learning-based information mining from ocean remote-sensing imagery. *National Science Review*, **7**(10): 1584-1605, https://doi.org/10.1093/nsr/nwaa047.

Li X F, Zhou Y, Wang F. 2022. Advanced information mining from ocean remote sensing imagery with deep learning. *Journal of Remote Sensing*, **2022**: 9849645, https://doi.org/10.34133/2022/9849645.

Li X L, Yang Y, Ishizaka J et al. 2023. Global estimation of phytoplankton pigment concentrations from satellite data using a deep-learning-based model. *Remote Sensing of Environment*, **294**: 113628, https://doi.org/10.1016/j.rse.2023.113628.

Liu H Q, Wei C Y, Lyu H et al. 2024a. Response of mineral particles in inland lakes to water optical properties and its influence on chlorophyll-*a* estimation. *Optics Express*, **32**(6): 9343-9361, https://doi.org/10.1364/OE.507956.

Liu T Y, Chen M S, Zhou M et al. 2019. Towards understanding the importance of shortcut connections in residual networks. *In*: Proceedings of the 33rd International Conference on Neural Information Processing Systems. Curran Associates Inc., Vancouver. 709p.

Liu X H, Warren M, Selmes N et al. 2024b. Quantifying decadal stability of lake reflectance and chlorophyll-*a* from medium-resolution ocean color sensors. *Remote Sensing of Environment*, **306**: 114120, https://doi.org/10.1016/j.rse.2024.114120.

Liu H Z, He X Q, Li Q Q et al. 2022. Evaluation of ocean color atmospheric correction methods for Sentinel-3 OLCI using global automatic in situ observations. *IEEE Transactions on Geoscience and Remote Sensing*, **60**: 1-19, https://doi.org/10.1109/TGRS.2021.3136243

Loisel H, Jorge D S F, Reynolds R A et al. 2023. A synthetic optical database generated by radiative transfer simulations in support of studies in ocean optics and optical remote sensing of the global ocean. *Earth System Science Data*, **15**(8): 3711-3731, https://doi.org/10.5194/essd-15-3711-2023.

Mamun M, Hasan M, An K G. 2024. Advancing reservoirs water quality parameters estimation using Sentinel-2 and Landsat-8 satellite data with machine learning approaches. *Ecological Informatics*, **81**: 102608, https://doi.org/10.1016/j.ecoinf.2024.102608.

Mobley C D. 1994. Light and Water: Radiative Transfer in Natural Waters. Academic Press, San Diego. 592p.

Mobley C D, Sundman L K. 2008. Hydrolight 5 Ecolight 5 Technical Documentation. Sequoia Scientific Inc, Bellevue. 95p.

Morel A. 1988. Optical modeling of the upper ocean in relation to its biogenous matter content (case I waters). *Journal of Geophysical Research*: *Oceans*, **93**(C9): 10749-10768, https://doi.org/10.1029/JC093iC09p10749.

Nechad B, Ruddick K G, Park Y. 2010. Calibration and validation of a generic multisensor algorithm for mapping of total suspended matter in turbid waters. *Remote Sensing of Environment*, **114**(4): 854-866, https://doi.org/10.1016/j.rse.2009.11.022.

Ondrusek M, Stengel E, Kinkade C S et al. 2012. The development of a new optical total suspended matter algorithm for the Chesapeake Bay. *Remote Sensing of Environment*, **119**: 243-254, https://doi.org/10.1016/j.rse.2011.12.018.

Ouillon S, Douillet P, Petrenko A et al. 2008. Optical algorithms at satellite wavelengths for total suspended matter in tropical coastal waters. *Sensors*, **8**(7): 4165-4185, https://doi.org/10.3390/s8074165.

Oyama Y, Matsushita B, Fukushima T et al. 2009. Application of spectral decomposition algorithm for mapping water quality in a turbid lake (Lake Kasumigaura, Japan) from Landsat TM data. *ISPRS Journal of Photogrammetry and Remote Sensing*, **64**(1): 73-85, https://doi.org/10.1016/j.isprsjprs.2008.04.005.

Pahlevan N, Mangin A, Balasubramanian S V et al. 2021. ACIX-Aqua: a global assessment of atmospheric correction methods for Landsat-8 and Sentinel-2 over lakes, rivers, and coastal waters. *Remote Sensing of Environment*, **258**: 112366, https://doi.org/10.1016/j.rse.2021.112366.

Pahlevan N, Smith B, Alikas K et al. 2022. Simultaneous retrieval of selected optical water quality indicators from Landsat-8, Sentinel-2, and Sentinel-3. *Remote Sensing of Environment*, **270**: 112860, https://doi.org/10.1016/j.rse.2021.112860.

Pahlevan N, Smith B, Schalles J et al. 2020. Seamless retrievals of chlorophyll-*a* from Sentinel-2 (MSI) and Sentinel-3 (OLCI) in inland and coastal waters: a machine-learning approach. *Remote Sensing of Environment*, **240**: 111604, https://doi.org/10.1016/j.rse.2019.111604.

Palmer M A, Bernhardt E S, Allan J D et al. 2005. Standards for ecologically successful river restoration. *Journal of Applied Ecology*, **42**(2): 208-217, https://doi.org/10.1111/j.1365-2664.2005.01004.x.

Paulino R S, Martins V S, Novo E M L M et al. 2025. Generation of robust 10-m Sentinel-2/3 synthetic aquatic reflectance bands over inland waters. *Remote Sensing of Environment*, **318**: 114593, https://doi.org/10.1016/j.rse.2024.114593.

Petzold T J. 1972. Volume Scattering Functions for Selected Ocean Waters. University of California, San Diego.

Pope R M, Fry E S. 1997. Absorption spectrum (380–700 nm) of pure water. II. Integrating cavity

measurements. *Applied Optics*, **36**(33): 8710-8723, https://doi.org/10.1364/AO.36.008710.

Prieur L, Sathyendranath S. 1981. An optical classification of coastal and oceanic waters based on the specific spectral absorption curves of phytoplankton pigments, dissolved organic matter, and other particulate materials. *Limnology and Oceanography*, **26**(4): 671-689, https://doi.org/10.4319/lo.1981.26.4.0671.

Renosh P R, Doxaran D, Keukelaere L D et al. 2020. Evaluation of atmospheric correction algorithms for sentinel-2-MSI and sentinel-3-OLCI in highly turbid estuarine waters. *Remote Sensing*, **12**(8): 1285, https://doi.org/10.3390/rs12081285.

Sadler J M, Appling A P, Read J S et al. 2022. Multi-task deep learning of daily streamflow and water temperature. *Water Resources Research*, **58**(4): e2021WR030138, https://doi.org/10.1029/2021WR030138.

Stöffelmair U, Popp T, Vountas M et al. 2025. Aerosol composition retrieval from a combination of three different spaceborne instruments: information content analysis. *Atmospheric Measurement Techniques*, **18**(9): 2005-2020, https://doi.org/10.5194/amt-18-2005-2025.

Stroud M K, Allen G H, Simard M et al. 2023. Optimizing satellite mission requirements to measure total suspended solids in rivers. *IEEE Transactions on Geoscience and Remote Sensing*, **62**: 4200409, https://doi.org/10.1109/TGRS.2023.3337641.

Wang H Y, Zhou Y F, Li X F. 2025. GDCM: generalized data completion model for satellite observations. *Remote Sensing of Environment*, **324**: 114760, https://doi.org/10.1016/j.rse.2025.114760.

Wirabumi P, Kamal M, Wicaksono P. 2021. Determining effective water depth for total suspended solids (TSS) mapping using PlanetScope imagery. *International Journal of Remote Sensing*, **42**(15): 5784-5810, https://doi.org/10.1080/01431161.2021.1931538.

Xue K, Boss E, Ma R H et al. 2019. Algorithm to derive inherent optical properties from remote sensing reflectance in turbid and eutrophic lakes. *Applied Optics*, **58**(31): 8549-8564, https://doi.org/10.1364/AO.58.008549.

Yin Z X, Wu P H, Li X Y et al. 2024. Super-resolution water body mapping with a feature collaborative CNN model by fusing Sentinel-1 and Sentinel-2 images. *International Journal of Applied Earth Observation and Geoinformation*, **134**: 104176, https://doi.org/10.1016/j.jag.2024.104176.

Zhou Y D, Yu K, Geng X E et al. 2024. Monitoring color for small water bodyies by fusing Sentinel-2 multispectral data and Gaofen-1 panchromatic imagery. *In*: IGARSS 2024-2024 IEEE International Geoscience and Remote Sensing Symposium. IEEE, Athens. p.4349-4353, https://doi.org/10.1109/IGARSS53475.2024.10640553.